

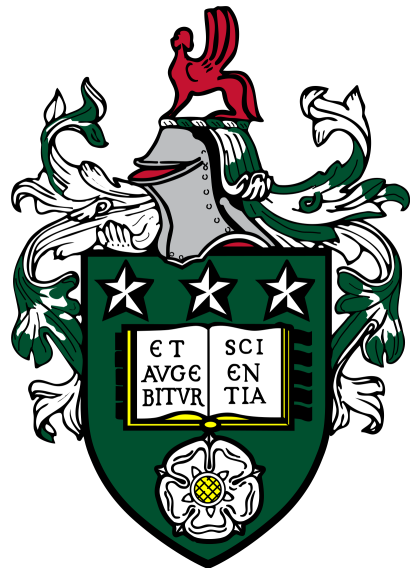
The Possibility of Detaching Viral Particles from a Disposable Face Mask

MECH5870M: Individual Report

Supervised by: Professor Andrew Bayly

Student Number: 201055860

Bradley Davy



School Of Computing

University of Leeds

Contents

1	Introduction	1
2	Literature Review	3
2.1	Modelling masks	3
2.2	Artificial Geometries	5
3	Method	6
3.1	Step 1 - The Python Script	7
3.2	Step 2 - The Blender Script	9
3.3	Step 3 - OpenFOAM	11
4	Results	13
4.1	Mesh Independence	13
4.2	Validation	14
4.3	2D simulations	16
4.4	3D Simulations	17
4.4.1	Velocity deviation	18
5	Discussion	22
5.1	The possibility of re-aerosylation	22
5.2	Packing density	23
5.3	Limitations	24
6	Conclusion	26

Nomenclature

α_i	Packing density of inner fibres
α_o	Packing density of outer fibres
α_p	porous medium permeability
Δm	Mask thickness
Δp	Pressure difference between the inlet and outlet
B_0	Zero order bessel function
C_2	Pressure-jump coefficient
C_d	Drag coefficient
C_p	orthogonality-index of non-woven filter media
d	Diameter of fibre
l	Mask layer thickness
l_f	Length of fibre
Re	Reynolds number
w	Domain cross section
<i>CFD</i>	Computational fluid dynamics
<i>DFM</i>	Disposable face mask
<i>SEM</i>	Scanning electron microscope

List of Figures

3.1	SEM images taken with a Carl Zeiss EVO MA15 SEM (beam voltage 5 kV, working distance 10 mm).	6
3.2	A schematic of the flow domain being simulated.	7
3.3	A schematic of the intersection of a fibre with the edge of the domain.	8
3.4	A single fibres intersection with the domain of interest.	9
3.5	Multiple fibres and there intersection with the domain.	9
3.6	From left to right, the first is the front view of the geometry file in Blender, the second is the side and the third is an angled profile.	10
3.7	A comparison of the SEM images with the artificial geometry. Both (a) and (b) are the filtering layer, (c) and (d) are the outer layer.	10
3.8	A snapshot of inside the mesh, showing the cell surfaces.	11
3.9	(a) shows the mesh before using snappyHexMesh, this is the rectangular mesh created using blockMesh, (b) shows the mesh after it has conformed to the .STL file.	12
4.1	The average velocity at the outlet plotted against the number of cells of the mesh. Mesh independent flow is to be found after 3,250,000 cells and thus is used through out all simulations.	13
4.2	A comparison of the pressure-velocity relationship of the geometries created in this report with models found in the literature.	14
4.3	The velocity induced through a mask given some pressure drop across the mask. Four different packing densities (α_i) are shown.	15
4.4	Velocity contour during a cough using a porous media model with α_p and C_2 from table 4.1, $\alpha_i = 0.15$	16
4.5	A contour plot of the pressure build up during a cough using a porous media model with α_p and C_2 from table 4.1, $\alpha_i = 0.15$	16
4.6	A 2D mesh generated as described in chapter 3.	17

4.7	The streamlines of the flow, coloured here by the velocity.	17
4.8	The streamlines as they pass through the top left hand corner of the domain, coloured here by the velocity.	17
4.9	A view of the streamlines at the outlet, coloured here by the velocity.	17
4.10	A contour plot of the domain, coloured here by the velocity.	18
4.11	A contour plot of the pressure variation through out the domain, the pressure drop which drives the flow can be clearly seen here.	18
4.12	A surface plot of the velocity at the outlet, located 100 μm from the end of the mask fibres.	18
4.13	Surface plots of the velocity at the outlet, located 100 μm from the end of the mask fibres. The letters correspond to those in table 4.2.	20
5.1	The critical detachment velocities for the 5 μm fibre with varying droplet size.	22
5.2	A plot of $\frac{1}{\alpha_p}$ against packing density.	23
5.3	A plot of C_2 against packing density.	23
5.4	An SEM image of the ouer layer of the mask, the melting junctions can be seen here. The red box highlights the size of the domain which has been simulated through out this report.	24
5.5	An SEM image of the inner layer of a used DFM.	25
5.6	An SEM image of the outer layer of a used DFM.	25

Chapter 1

Introduction

Infectious diseases have plagued societies for as long as they have existed. Modern science has shed light on the way that these diseases spread and how they affect the body. The spread of many viral infections is now attributed to droplets, which carry a viral load, coming from the mouth and nose of infected individuals. Since the outbreak of COVID-19, the clinical disease related to the infection of SARS-CoV2 coronavirus, there has been an increase of studies carried out to determine the effectiveness of different preventative measures. These preventative measures aim to reduce the amount of viral droplets which leave one person and enter another. One method which has been used globally is the wearing of face masks in public places. Face masks offer both inwards and outwards protection by stopping viral particles passing in and out of the mask. In order to understand how effective face masks can be, many have turned to computational fluid dynamics (CFD). This tool allows researchers to understand the flow of air during typical human activity, like breathing, and thus determine the path of viral particles leaving an individuals mouth or nose.

One problem which has had little exposure in the surrounding literature is the affect that wearing a mask has on the mask itself. In particular, if, after wearing a mask for a prolonged length of time, a sudden exhalation is able to detach collected viral particles/droplets. Henceforth, this process will be referred to as re-aerosilisation. With the use of masks becoming increasingly common, the risk of re-aerosilisation is still unclear.

The focus of this study is to determine if a cough is able to re-aerosilise any viral particles. A cough is used as this is characterised by a violent exhalation which may increase the probability that re-aerosilisation will occur. In order to determine if a droplet will detach, two things must be known; the velocity at which a droplet will detach and the velocity field inside a mask. In most large scale simula-

tions an approximation is used in order to determine the average velocity through a mask. Despite the usefulness of this approximation, this study shows that it ultimately fails to capture significant features of the flow.

In this study a robust method is adapted to make, to the authors knowledge, a novel disposable face mask (DFM) geometry. A DFM was chosen as they are widely available and have become common place across many areas of the globe. Specifically, a $400\text{ }\mu\text{m}$ by $400\text{ }\mu\text{m}$ cross section of the mask was generated and the surrounding air flow determined via the use of CFD. In this study the fibres of the masks themselves were created using a three step process. All software utilised in the study is freely available and open source. All scripts discussed during this report can be found at <https://github.com/Brad-Davy/Fibres>.

Once created, the relationship between the pressure drop across the mask and the velocity through the mask was explored. This relationship was then compared to the models used in the literature, which showed a similar profile. The pressure-velocity relationship was then utilised in a macro-scale CFD simulation. It was determined, during a cough, that the maximum pressure behind a DFM was 51.5 Pa. The DFM geometries were then simulated on using this pressure difference. From this, the flow field through a mask was determined during a cough. Six individual geometries were created and the flow through them determined. On average the maximum velocity in the mask was 8 times higher than the average velocity. This is then discussed in relation to how this affects the possibility of re-aerosilisation to ultimately understand the risk it poses.

Chapter 2

Literature Review

Many viral and bacterial infections such as influenza [1], tuberculosis [2] and SARS-CoV-2 [3] are transmitted via droplets expelled from an infected individual. These droplets are typically expelled from the nose and mouth during breathing, coughing and sneezing [4]. Since the outbreak of COVID-19 many studies have been carried out to determine effectiveness of different preventative measures [5]. The key aim of these measures is to reduce the likelihood of droplets with a viral load being transmitted to other individuals. As such, the wearing of face masks has been widely accepted by the global community, with it being mandated by law in various countries [6].

2.1 Modelling masks

Many studies have ascertained the effectiveness of face masks through the use of CFD. Due to the size of the fibres in the mask, an approximation must be used to try and understand the effect it has on the flow. Trying to directly model the fibres themselves and then the flow field of the wider environment would require too many computational cells. To circumnavigate this problem, a variety of methods have been developed in order to account for the mask. Khosronejad *et al.* [7] model the affect of the mask by applying a drag force to the flow at the unstructured grid points where the mask is located. In this study two different masks (medical and non-medical) were simulated by applying different drag coefficients. The medical grade mask had a larger drag coefficient and thus slowed the flow down more. The authors found a significant reduction in the distance travelled by droplets (2.14 m) when wearing a medical grade mask[7]. Other studies use an alternative approach, where the mask is modeled as a porous media and the flow through the mask is determined by either equation 2.1 or 2.2,

$$\Delta p = -\frac{\mu}{\alpha} u \Delta m, \quad (2.1)$$

$$\Delta p = -\left(\frac{\mu}{\alpha_p} u + \frac{1}{2} C_2 \rho u^2\right) \Delta m. \quad (2.2)$$

Where,

$$\mu = \text{fluid viscosity (air)} = 1.789 \times 10^{-5} \text{kgm}^{-1}\text{s}^{-1},$$

$$\rho = \text{fluid density (air)} = 1.204 \text{kgm}^{-3},$$

$$\alpha_p = \text{porous medium permeability},$$

$$C_2 = \text{pressure-jump coefficient},$$

$$u = \text{velocity (normal to the porous face)},$$

$$\Delta p = \text{pressure drop across the mask},$$

$$\Delta m = \text{thickness of mask}.$$

The linear term comes from Darcy's Law and the non-linear term from inertial losses. Table 2.1 summarises the different methods utilised in different studies. Most studies opt to use a form of Darcy's law, some with the second order term added for inertial losses.

Study	Method	Constants
Zhang <i>et al</i> [8]	Darcy's law	$\alpha = 8.93 \times 10^{-11}$
Dbouk <i>et al</i> [5]	Darcy with inertial losses	$\alpha = 8.14 \times 10^{-10}$, $\Delta m = 2 \text{ mm}$, $C_2 = 610$
Khosronejad <i>et al</i> [7]	Drag coefficient	$\Delta m = 2.2 \text{ mm}$, $C_d = 600$, $C_d = 350$
Davy	Fibre Model	$\Delta m = 0.25 \text{ mm}$
Lei <i>et al</i> [9]	Darcy's law	$\alpha = 8.93 \times 10^{-11}$
Zhu <i>et al</i> [10]	Darcy's law	$\alpha = 8.93 \times 10^{-11}$, $\Delta m = 4 \text{ mm}$
Kumar <i>et al</i> [11]	Darcy's law	$\alpha = 8.93 \times 10^{-11}$, $\Delta m = 4 \text{ mm}$

Table 2.1: A summary of the current studies which simulate flow through a mask.

As table 2.1 highlights there has been a plethora of studies which utilise different methods to model the air flow through a mask. It can also be seen here that the models often opt for a mask thickness of the order of a few mm. Where as a DFM, as identified by Leonas *et al.* [12], typically have thicknesses less than 1 mm. In each case, the average air-flow is determined but the fine structure of the air-flow is unknown. In order to determine the possibility of re-aerosylation, the variations from this average must also be understood.

Early work on re-aerosolisation was conducted by Qian *et al.* [13, 14], in these studies experimental set ups were created in order to re-aerosolise particles from a N95 mask. In these studies, it was found that the possibility of re-aerosolisation depended solely on the air velocity through the filter of the mask, with most particles that did detach being on the smaller size ($3\text{ }\mu\text{m}$ - $5\text{ }\mu\text{m}$). It was also found that re-entrainment increases with the square of the particle diameter. This further shows the need to determine the flow in a mask, although the average may be below the detachment velocity there could be sections of the mask which experience higher velocities.

2.2 Artificial Geometries

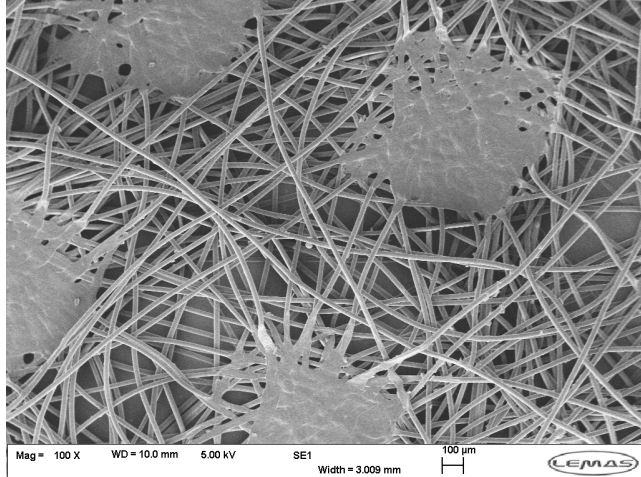
In order to model the air-flow through a mask, the mask fibres themselves must be meshed so that CFD simulations can be ran to determine the surrounding air flow. In other fields, like textiles, the generation of these geometries has been done for some time. Some studies generate filter geometry files by extracting a 3D geometry from 2D images. Lehmannn *et al.* [15] present a method which used X-ray CT scan images to reconstruct 3D geometry files of a filter media. Some studies embed the filter in a resin, then 2D slices are taken and reconstructed into a 3D digital object [16]. A multitude of studies create virtual geometries [17, 18, 19], by exploiting different statistical distributions the fibres can be laid down (virtually) in orientations which best match real filters. However, none of the above methods have been utilised to understand the flow through a DFM. Thus far, the modelling of masks has been confined to a boundary condition (equations 2.1 and 2.2), as the point of import is the flow of air after passing through the mask. In this study virtual fibres were made due to the flexibility that this method offers. It is possible to generate multiple different geometries and allows for the optimisation of mask design. On top of this, it makes possible an exploration of parameter space which would otherwise be un-attainable.

This study hopes to show that, while necessary to reduce computational complexity, the use of simplifying models misses out on key flow details. It also makes the first step towards modelling how particles are being trapped in DFM and the risk they pose in regards to re-aerosylation. Having a robust virtual geometry paves the way for future work on the small scale processes which occur within masks, and allows for the optimisation of parameters like packing density, fibre size and mask thickness.

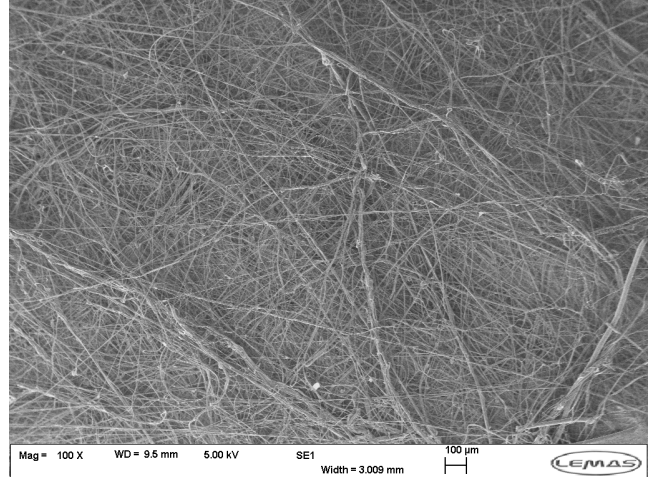
Chapter 3

Method

In order to determine the airflow through a DFM, a geometry of the mask fibres must be generated. The 3 layers of the mask are identified in work carried out by Yatin Darbar [20] and mirrored by Battegazzore *et al* [21], the inner and outer layers were both made up of $40\text{ }\mu\text{m}$ fibres, shown in figure 3.1 (a). Then the central, filtering, layer is made up of a variation of fibre diameters ($d \in (3\text{ }\mu\text{m}, 15\text{ }\mu\text{m})$), as shown in figure 3.1 (b).



(a)



(b)

Figure 3.1: SEM images taken with a Carl Zeiss EVO MA15 SEM (beam voltage 5 kV, working distance 10 mm).

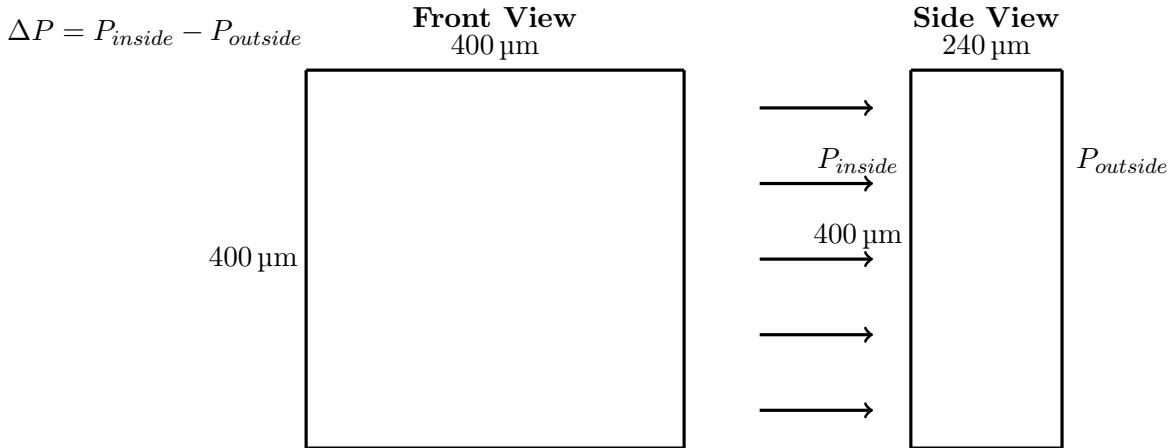


Figure 3.2: A schematic of the flow domain being simulated.

In order to determine the air flow through a mask, a 400 μm by 400 μm section of the mask is generated and the air flow through simulated. A 400 μm domain was chosen in order to both identify key flow details whilst also being able to capture the bulk properties of the mask like the relationship between velocity and pressure. It was found that typical blue 3-ply surgical masks (3-ply, pleated cellulose polypropylene, polyester) have a thickness of 234 μm [12]. As such, the mask geometries generated in this study had a thickness between 240 μm – 335 μm . The reason for the variation is due to the random way in which the fibres are created and will be explained in further detail in section 3.2.

A method developed by Abishek *et al.* [22] is modified in order to create the geometry files. The mesh creation is split into 3 principal categories, first the skeleton of the fibre geometry is made in Python (`Fibrous.py`). During this step the thickness, angle and center-point of each fibre is determined. Then cylinders are created at the specified center-points, angles and thicknesses (`Blender.py`). Finally the meshes are generated using a variety of utilities in OpenFOAM.

3.1 Step 1 - The Python Script

The Python script first takes input parameters from the user, the fibre diameter (d), inner packing density (α_i), outer packing density (α_o), the domain cross section (w), the thickness of the layer (l) and finally the length of the fibre (l_f). Following this, the script generates a single fibre within the specified domain. Since there are three layers in a typical DFM [20, 21] the script creates each section separately. Later they were offset from one and other in Blender. In line with the findings of Battegazzore *et al.*, [21] when creating the outer fibres the diameter is set to 40 μm . Where as, when generating the filter fibres the fibre diameter is randomised in the range $d \in (3 \mu\text{m}, 15 \mu\text{m})$. Once created, the fibre is then moved by some

distance \mathbf{r} where,

$$\mathbf{r} \in ((0, l)\hat{i} + (-w/2, w/2)\hat{j} + (-w/2, w/2)\hat{k}). \quad (3.1)$$

In the case of a DFM, these were set to $w = 400 \mu\text{m}$ and $l = 80 \mu\text{m}$. Given these ranges are in the $(\hat{i}, \hat{j}, \hat{k})$ directions, random values were selected using Python's "Random" library. The fibres were then rotated through an angle β such that they follow a Von-Mises distribution given by equation 3.2.

$$f(\beta|C_p) = \frac{e^{C_p \cos(\beta)}}{2\pi B_0 C_p}. \quad (3.2)$$

In equation 3.2, B_0 is the zero order Bessel function and C_p is the orthogonality-index of non-woven filter media. In this study, $C_p = 0.01$ as there is no preferred orientation of the fibres and thus the distribution is similar to a random distribution. Now the fibre has been moved and rotated, only part of the fibre still remains in the domain. This new length must be calculated in order to determine α_o and α_i . In Python, the fibre itself is defined by an angle and a central point. Given that the length of the fibre is known, the location of the start and end points of the fibre can be determined. From these 3 points a linear fit can be made to the fibre. Given the line is of the form $y = mx + c$ the intercept between the line and the edges of the domain can be determined, then using Pythagoras the length of the line which is in the domain can be established. However, this means that the cylinder is approximated to be straight at the edge of the domain as illustrated in figure 3.3.

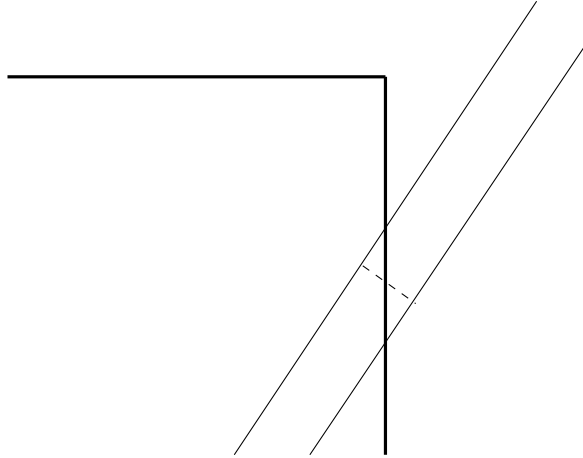


Figure 3.3: A schematic of the intersection of a fibre with the edge of the domain.

An example of a single fibre located in the domain is shown in figure 3.4 with the edges noted by black points. Once the length of the fibre is known the volume of said fibre can be determined. This process is then repeated until the required packing density is met, figure 3.5 shows the case of the packing density being set to 0.1. The 3 layers are constructed separately and then written to separate text files which can then be read during the next step.

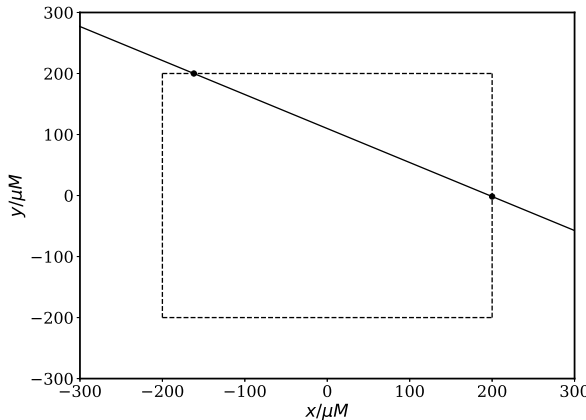


Figure 3.4: A single fibres intersection with the domain of interest.

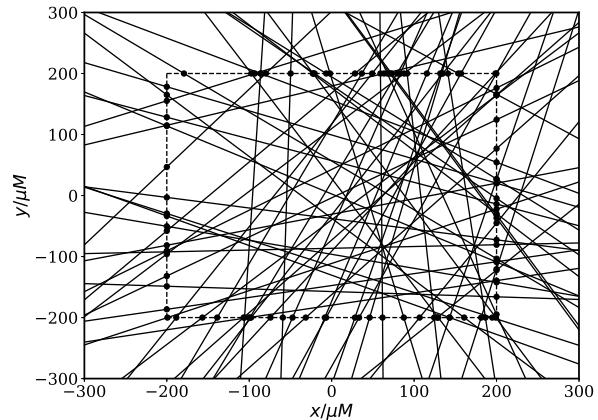


Figure 3.5: Multiple fibres and there intersection with the domain.

3.2 Step 2 - The Blender Script

Once the input files have been generated, the Blender script can be ran to generate the full geometry file. The Blender script first reads in the position of each fibre, there angle and there diameter. It then generates a cylinder at each position with the given angle and diameter. The 3 layers are offset from one another to create a real mask geometry. After the geometry was created in blender it was then exported as a Stereo-lithography (.STL) file. This file can then be used by multiple OpenFOAM utilities in order to construct a 3D mesh.

A visual comparison between the artificial geometry and a SEM image of the real geometry is shown in figure 3.7, both show a $400\text{ }\mu\text{m}$ cross sections. Comparing figure 3.7 (a) and (b) it can be seen that there are reasonable similarities between the two. The same can be said for (c) and (d) which shows the inner layer. Also shown, in figure 3.6 is the three layers after they have been combined together in Blender. Each layer is around $80\text{ }\mu\text{m}$ thick, but as displayed in figure 3.6 the layers can be thicker. This is most evident when considering the side profile (middle image of figure 3.6). This is due to the fact the center-point of the fibre can be moved a distance of $80\text{ }\mu\text{m}$. Since the center-point can be located at $80\text{ }\mu\text{m}$ the edge of the cylinder can extend $\frac{d}{2}$ further. In this case, the maximum possible thickness of the two outer layers is $120\text{ }\mu\text{m}$ and the maximum thickness of the middle layer $95\text{ }\mu\text{m}$, giving a total possible variation of $95\text{ }\mu\text{m}$ in total thickness.

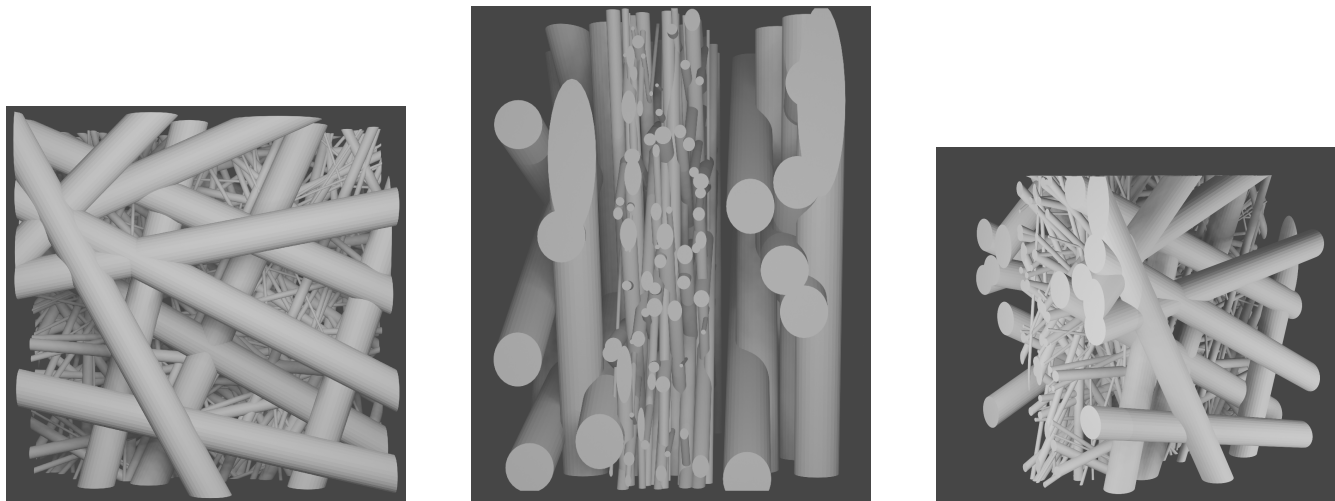


Figure 3.6: From left to right, the first is the front view of the geometry file in Blender, the second is the side and the third is an angled profile.

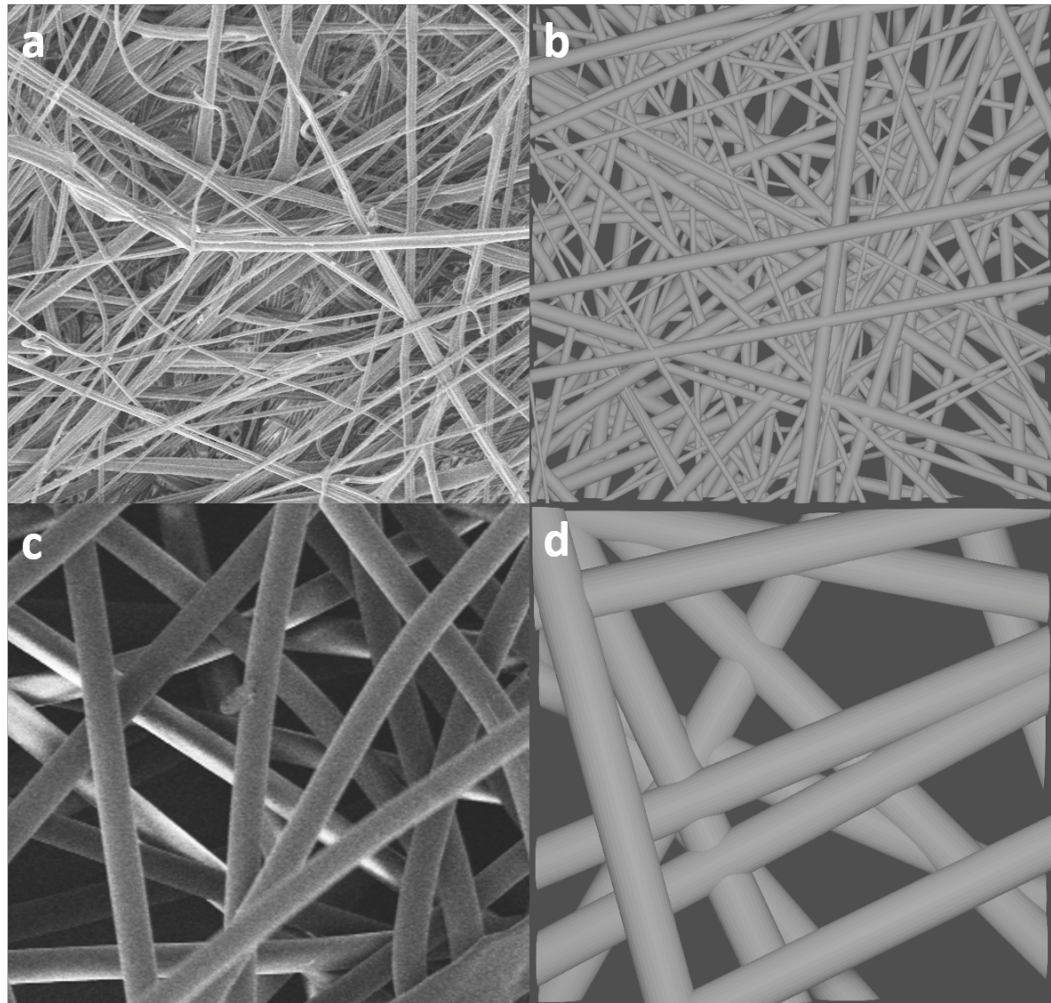


Figure 3.7: A comparison of the SEM images with the artificial geometry. Both (a) and (b) are the filtering layer, (c) and (d) are the outer layer.

3.3 Step 3 - OpenFOAM

After the .STL file has been generated, a selection of utilities in OpenFOAM were used in order to create a mesh which is adequate for CFD simulations. First a rectangular mesh is generated using the `blockMesh` utility. The number of divisions in the (x, y, z) directions are defined here. The number of divisions were modified to control the overall cell count of the mesh. After the rectangular mesh has been generated, the surface features of the .STL file can be extracted using the utility `surfaceFeatureExtract`. The mesh was then iteratively modified so that it conforms to the surface of the .STL file. This is done with the utility `snappyHexMesh`, the resultant meshes are shown in figures 3.8 & 3.9.

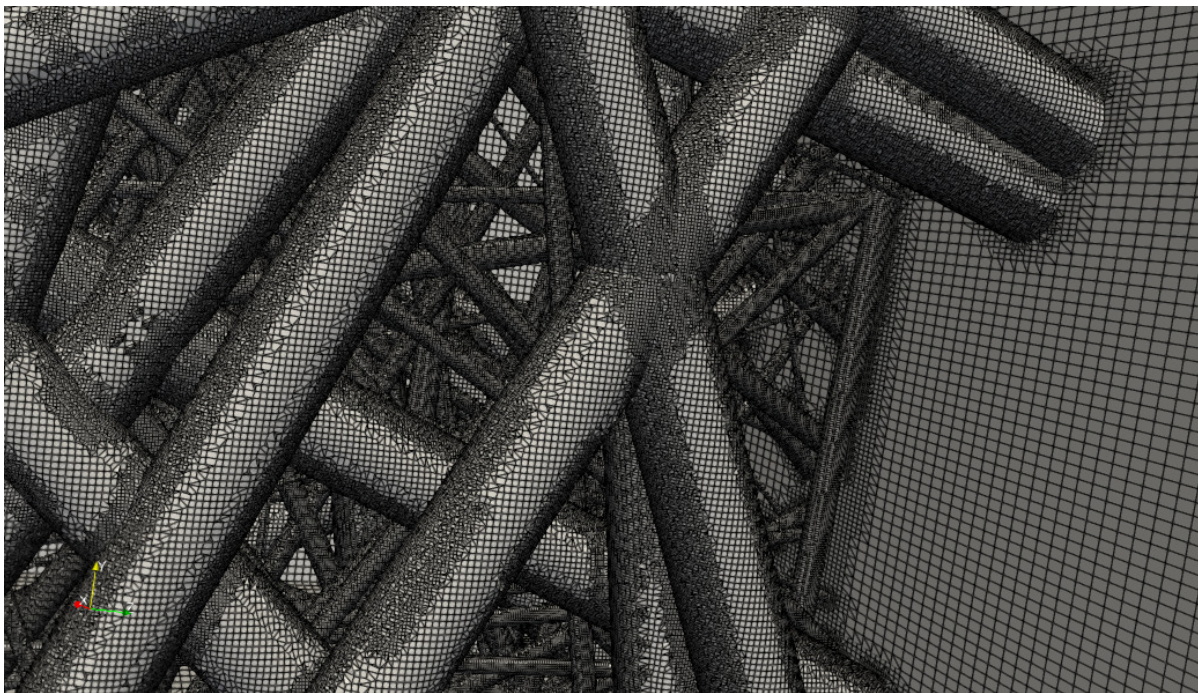


Figure 3.8: A snapshot of inside the mesh, showing the cell surfaces.

Once the mesh has been generated, OpenFOAM's `checkMesh` function was used to determine the quality of the mesh. Once checked, the mesh is transformed such that it is at the correct scale for the problem. It was found that in order to create the best mesh it is best to create the mesh on the order of meters and then later transform it by using the `transformPoints` utility. An example case file can be found at <https://github.com/Brad-Davy/fibres/Geom4>.

After the mesh has been generated the Navier-Stokes (equation 3.4) and the continuity equation (equation 3.3) were solved throughout the domain. The flow is assumed to be incompressible, isothermal and steady. This was done using OpenFOAM's `simpleFoam` solver. This solver utilises the semi-implicit method for pressure linked equations (SIMPLE) algorithm. The inherent non-linearity of the Naver-Stokes

equations is dealt with by using the velocity field the iteration before.

$$\nabla \cdot \mathbf{u} = 0. \quad (3.3)$$

$$\mathbf{u} \cdot (\nabla \cdot \mathbf{u}) = -\frac{1}{\rho} \nabla P + \mu/\rho \nabla^2 \mathbf{u}. \quad (3.4)$$

Where, \mathbf{u} is the velocity of the flow, P is the pressure, μ is the viscosity and ρ is the density. In all simulations $\mu = 1.81 \times 10^{-5} \text{ kg/m s}$ and $\rho = 1.225 \text{ kg m}^{-3}$. Equation 3.4 is solved first which creates a velocity solution which is in general not divergence free ($\nabla \cdot \mathbf{u} \neq 0$). Then using both equations 3.3 and 3.4 a pressure field is constructed which, if inserted into the Navier-Stokes equation, delivers a divergence free solution. The velocity field is updated accordingly. This method is carried out using a finite volume scheme. A laminar solver was used as the Reynolds number (Re) of this flow was typically quite small. Given by,

$$Re = \frac{UL\rho}{\mu}. \quad (3.5)$$

Where U is the maximum velocity in the flow, L is the characteristic length of the flow. Given the largest fibre used was $40 \mu\text{m}$ the Re was of the order of 10.

The choice of the boundary conditions were chosen in order to match the physical conditions present whilst wearing a mask. As such, the surrounding walls of the domain were set to slip conditions. The mask fibres themselves were set to no-slip. Since flow through a mask is caused by the difference in pressure inside and outside the mask; the flows simulated here were pressure driven flows. The pressure was specified on the outlet to be atmospheric (101325 Pa), then by specifying an inlet pressure, a pressure drop across the mask fibres is induced.

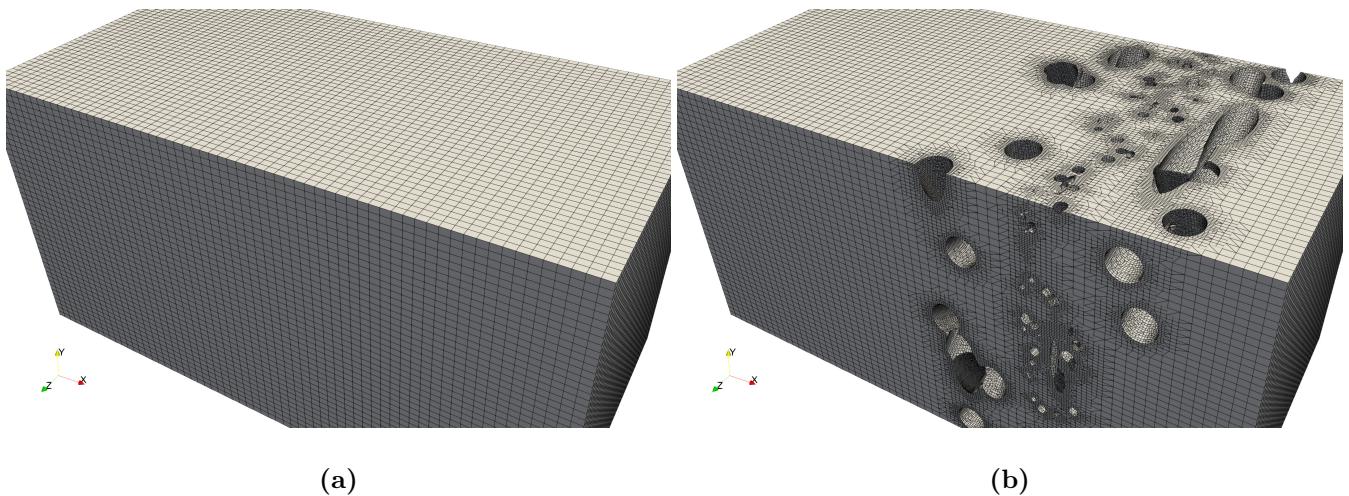


Figure 3.9: (a) shows the mesh before using snappyHexMesh, this is the rectangular mesh created using blockMesh, (b) shows the mesh after it has conformed to the .STL file.

Chapter 4

Results

4.1 Mesh Independence

A mesh independence study was carried out setting $\alpha_i = 0.25$ and $\alpha_o = 0.4$. The key parameter of concern regarding this flow is the average velocity at the outlet, as such this was monitored for gradually increasing cell count. Figure 4.1 shows that mesh independent flow is first achieved after 3,250,000 cells. As such, this size mesh is used through out the remaining simulations. The choice to set $\alpha_i = 0.25$ was made as this was the highest used through out the study. Thus, if the mesh is independent at this packing density it is assumed to be independent for other, less packed, geometries.

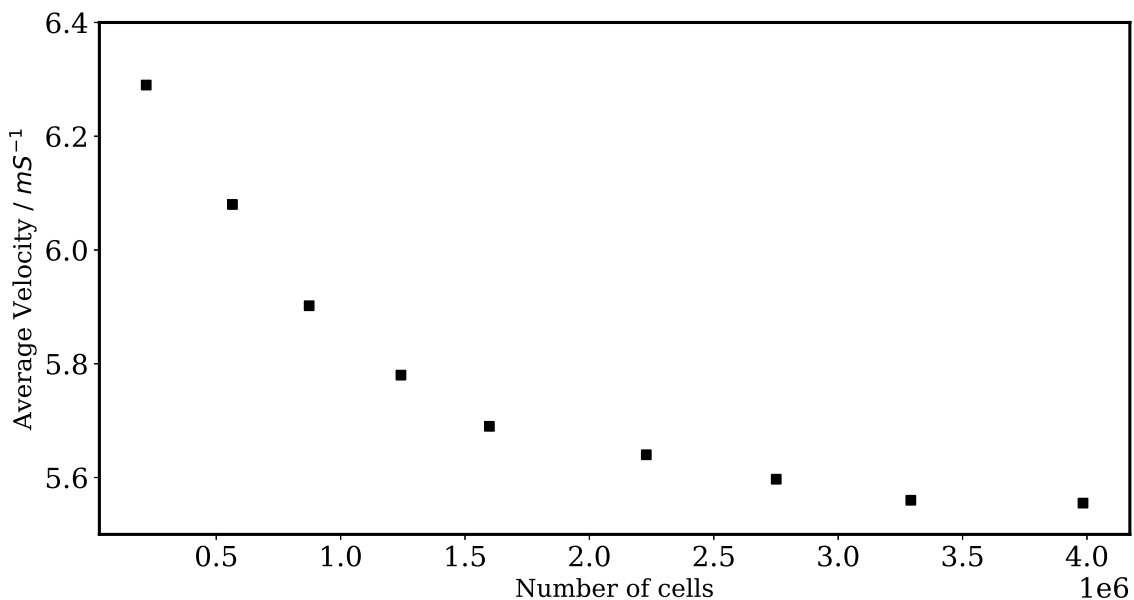


Figure 4.1: The average velocity at the outlet plotted against the number of cells of the mesh. Mesh independent flow is to be found after 3,250,000 cells and thus is used through out all simulations.

4.2 Validation

To ensure that the geometry created was in fact producing similar results to those in the literature, four geometries were produced. All had the same inner and outer layer, but the middle filtering layer was adjusted to see the affect this had on the mask. As such, α_i was varied between 0.1 and 0.25 and shown in 4.2. The models used in the literature and highlighted in table 2.1 are compared to the results of this study in figure 4.2.

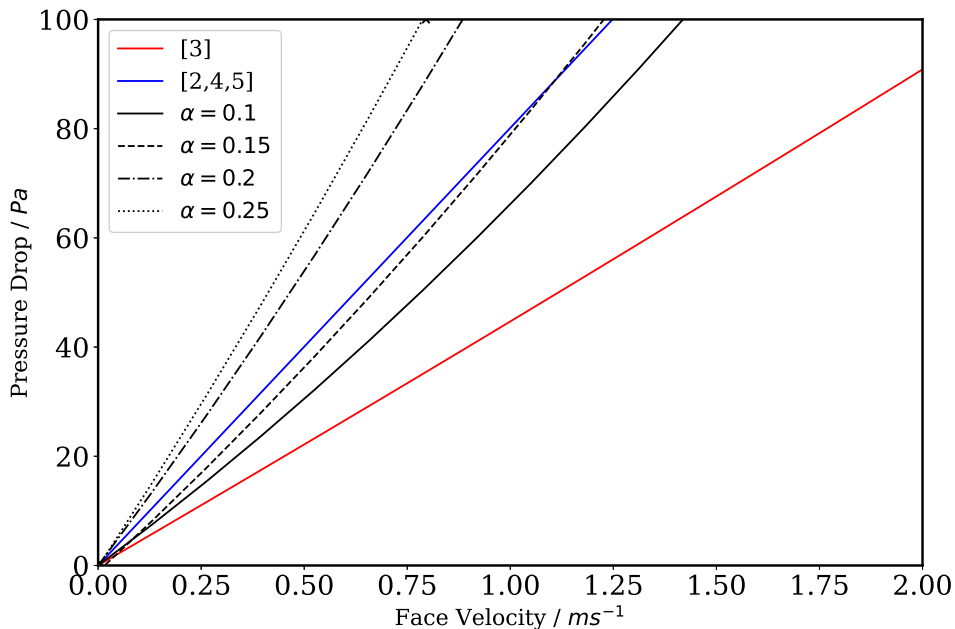


Figure 4.2: A comparison of the pressure-velocity relationship of the geometries created in this report with models found in the literature.

The comparison is limited to 100 Pa as this is the upper limit of pressure drops induced during a cough, this is later shown in figure 4.5. As can be seen in figure 4.2 there is reasonable overlap between the model created here and the models used in the larger simulations. This provides confidence in the geometry files, showing that the velocity fields produced are inline with those currently used in the literature.

In order to use this data in a larger scale simulation a similar approach is used to that found in the literature [5]. As such, a quadratic must be fit to the data and both α_p and C_2 must be determined in equation 2.2, given by,

$$\Delta p = -\left(\frac{\mu}{\alpha_p} u + \frac{1}{2} C_2 \rho u^2\right) \Delta m.$$

To this end, the pressure-velocity curve for each packing density was further explored, this is shown in

figure 4.3. Then using a mask thickness of 300 μm the constants α_p and C_2 can be determined, as shown in table 4.1.

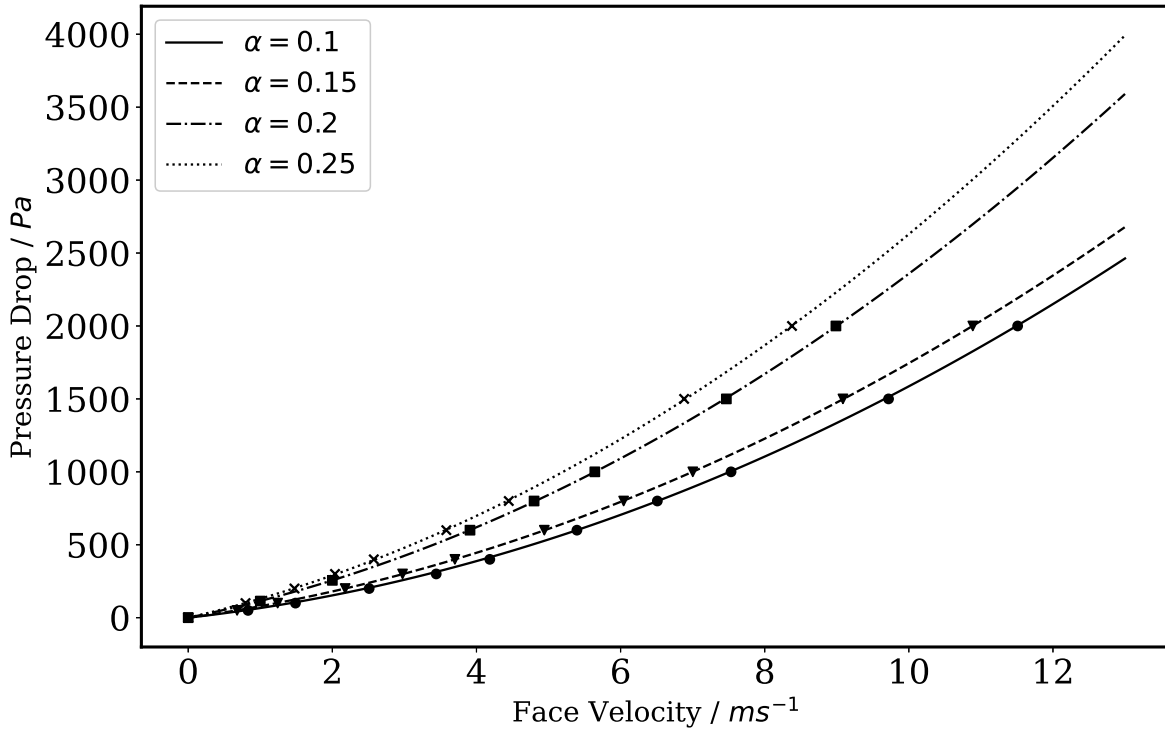


Figure 4.3: The velocity induced through a mask given some pressure drop across the mask. Four different packing densities (α_i) are shown.

α_i	$\alpha_p / \times 10^{-11} \text{m}^2$	$C_2 / \times 10^4 \text{m}^{-1}$
0.1	9.6	6.9
0.15	7.7	7.0
0.2	5.3	8.9
0.25	4.6	9.8

Table 4.1: A table showing the constants α_p and C_2 for masks with different inner packing densities (α_i).

As displayed in figure 4.3, changing the packing density of the inner mesh has an affect on the relationship of pressure and velocity. Alexander Lang utilised the porous jump model using the parameters from the $\alpha_i = 0.15$ case. By conducting a CFD simulation of a cough it was determined that the maximum pressure that is created behind a mask during a cough is 51.5 Pa [23]. Details of this work can be found

within Alexander Lang's report. These simulations of a cough can be seen in figures 4.4 & 4.5.

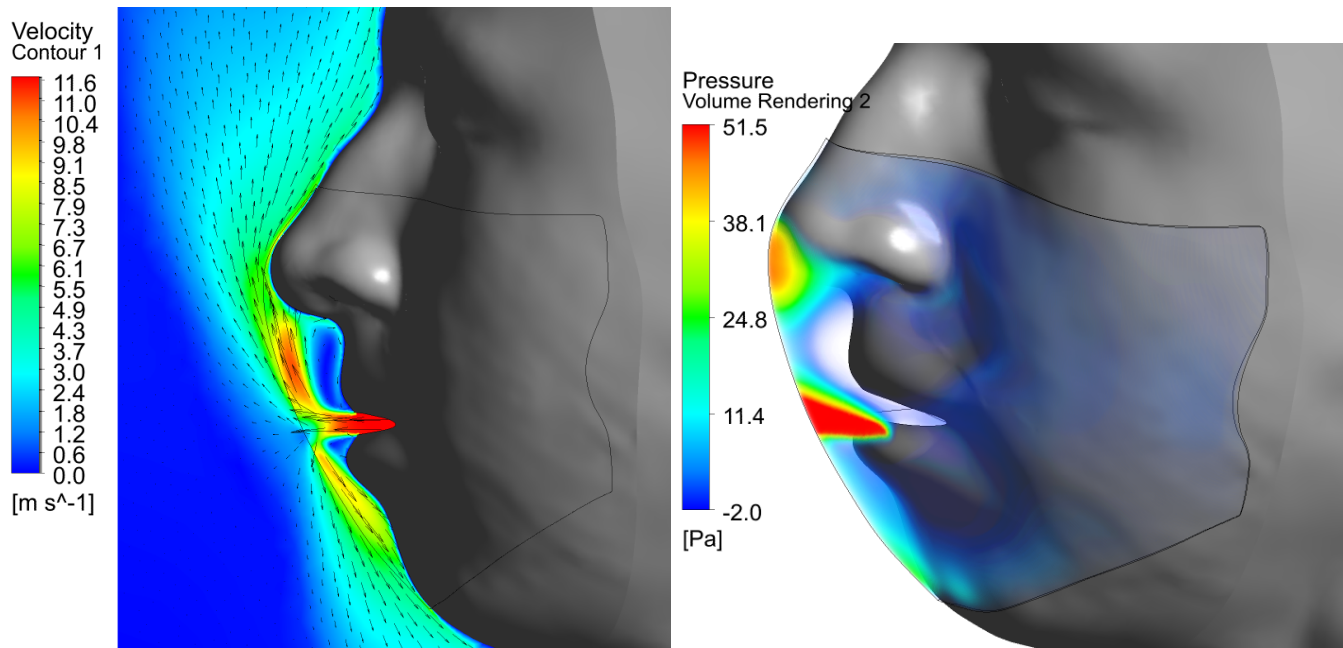


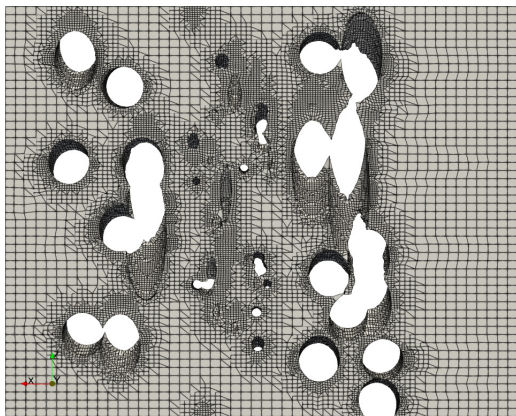
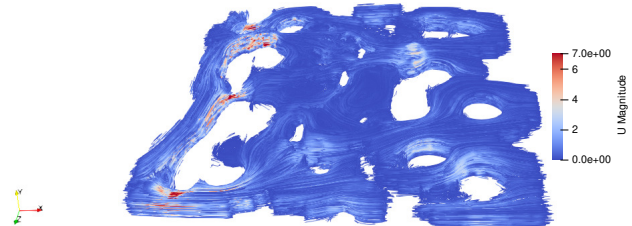
Figure 4.4: Velocity contour during a cough using a porous media model with α_p and C_2 from table 4.1, $\alpha_i = 0.15$.

Figure 4.5: A contour plot of the pressure build up during a cough using a porous media model with α_p and C_2 from table 4.1, $\alpha_i = 0.15$.

4.3 2D simulations

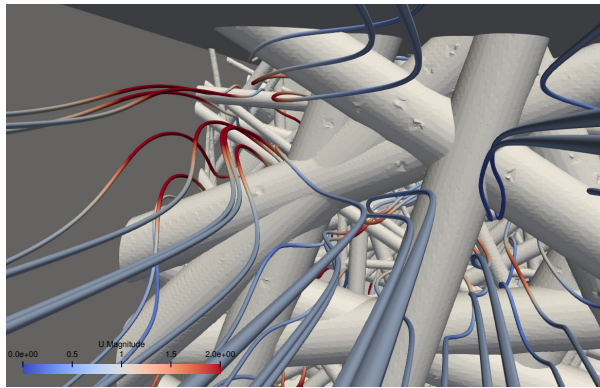
Now the maximum pressure drop across a mask during a cough has been determined, the flow field at this pressure can be understood. Initial simulations were carried out on a 2D slice of the 3D mesh. The 2D mesh was generated as laid out in chapter 3, however it is reduced to a single cell in the z direction. The resultant mesh is shown in figure 4.6. A 2D mesh was first used in order to better understand how the flow is moving around the fibres themselves. On top of this, the 2D mesh allowed for faster simulations so that any errors could be rectified in a shorter amount of time. A pressure drop of 50 Pa was established across the fibres and the resultant flow is shown in figure 4.7. It can be seen in figure 4.7 that the flow has a maximum velocity when passing between the fibres and the flow is severely contorted as it moves through the domain. This is to be expected due to conservation of mass and momentum.

After running the initial simulations in 2D, much larger meshes were made in 3D and ran on a high performance computer (ARC4). Simulations were ran on 12 cores, typically having a cell count of above 3,000,000. Examples of these simulations can be found in figures 4.8, 4.9, 4.10 & 4.11.

**Figure 4.6:** A 2D mesh generated as described in chapter 3.**Figure 4.7:** The streamlines of the flow, coloured here by the velocity.

4.4 3D Simulations

In the 3D case, the pressure drop was again set to 50 Pa and the resultant flow is shown in figures 4.8, 4.9, 4.10 & 4.11. This time the full 400 μm by 400 μm is used. Much like the 2D case the streamlines are severely contorted by the mask fibres. Figures 4.8 & 4.9 both show that the streamlines change dramatically when passing through the mask. Also mirroring the results seen in the 2D case, the flow is at its peak velocity when passing through the fibres. Figure 4.8 shows the streamlines as they pass through the top left corner of the domain, again highlighting the distortion and increase in velocity which occurs during the passage through the mask.

**Figure 4.8:** The streamlines as they pass through the top left hand corner of the domain, coloured here by the velocity.**Figure 4.9:** A view of the streamlines at the outlet, coloured here by the velocity.

4.4.1 Velocity deviation

It is interesting to note the difference between the maximum and average velocity in the flow. This can be easily observed by considering the velocity at the surface of the domain. Figure 4.10 shows how the velocity changes throughout the domain, with the maximum velocity being 4.1 m s^{-1} . Comparing this with the average velocity of 0.66 m s^{-1} , it can be seen that there is a significant difference. This is further highlighted by looking at the velocity field at the outlet (figure 4.12). There is a clear variation in the flow, with two peaks at either side of the domain.

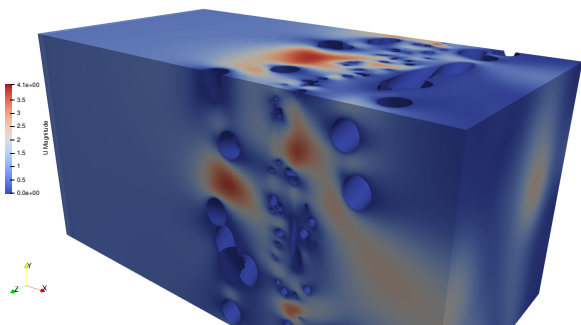


Figure 4.10: A contour plot of the domain, coloured here by the velocity.

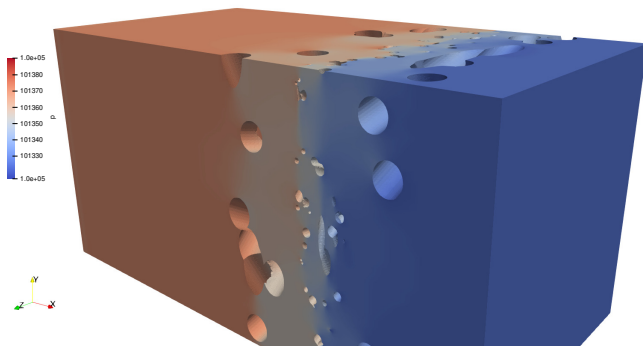


Figure 4.11: A contour plot of the pressure variation through out the domain, the pressure drop which drives the flow can be clearly seen here.

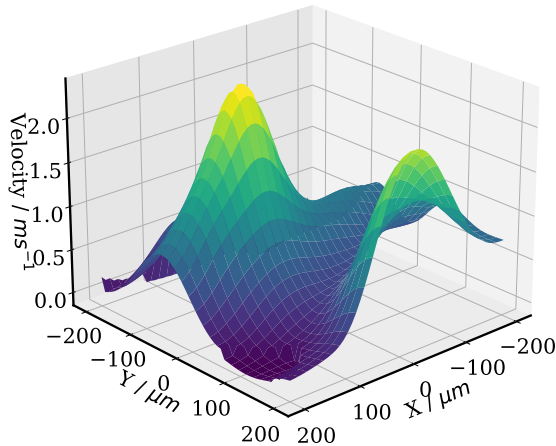
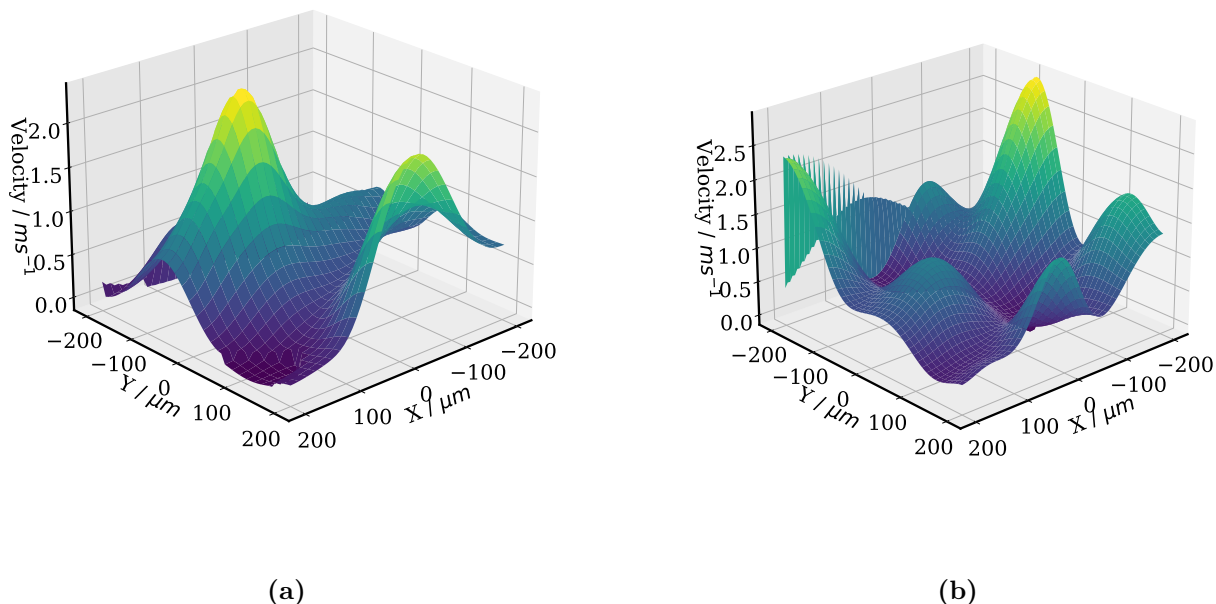


Figure 4.12: A surface plot of the velocity at the outlet, located $100 \mu\text{m}$ from the end of the mask fibres.

This variation could possibly be caused by this specific geometry file, rather than a feature which exists across a DFM. In order to show that the deviations from the mean flow were consistent to more than one geometry, 6 different geometries were created. Setting $\alpha_o = 0.4$ and $\alpha_i = 0.15$ for all 6 geometries. A pressure drop of 50 Pa is again induced across the fibres and the resulting flows were determined using OpenFOAM's simpleFoam solver. In order to deduce the variation of velocity in the flow, both the average and maximum velocities are noted in table 4.2. On top of this, a surface plot of the velocity at the outlet is also plotted for each individual geometry.

Geometry	Cell Count	Avg Velocity / $m s^{-1}$	Max Velocity / $m s^{-1}$
a	3,193,473	0.66	4.2
b	2,703,513	0.77	4.9
c	2,781,137	0.75	4.7
d	2,800,051	0.54	4.4
e	2,923,216	0.61	7.4
f	2,948,041	0.47	5.0

Table 4.2: A table showing the average and maximum velocity through a mask for 6 randomly generated fibre geometries.



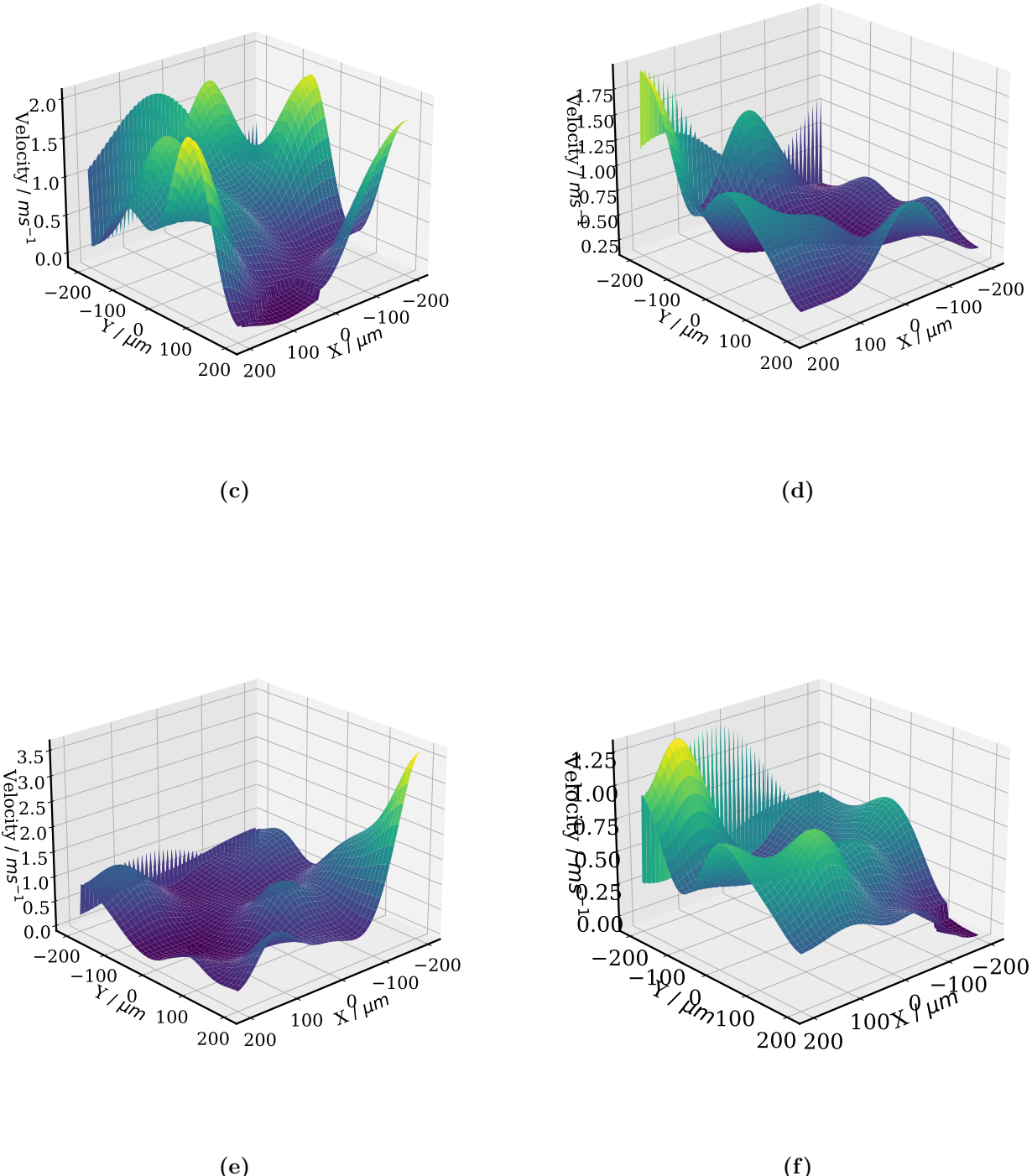


Figure 4.13: Surface plots of the velocity at the outlet, located 100 μm from the end of the mask fibres. The letters correspond to those in table 4.2.

With the outlet being located around 100 μm from the end of the mask, this gives a good representation of the velocity field as it leaves the mask. It is interesting to see in table 4.2 that the maximum velocity

is, on average, 8 times larger than the mean velocity of the flow. Although this significant variation only occurs in a small section of the mask, there is still significant variation at the outlet, shown by figure 4.13. It seems that this variation is the rule rather than the exception and is likely to persist across much of the mask.

Chapter 5

Discussion

5.1 The possibility of re-aerosylation

In order to assess the possibility of re-aerosylation two key factors must be established, the velocity through a mask and the velocity at which droplets detach. This study has determined the velocity field through a mask. It has been established that there is significant variation in the maximum and average velocity. Work conducted by Ciara Higham [24] has determined the detachment velocity of varying sizes of particles.

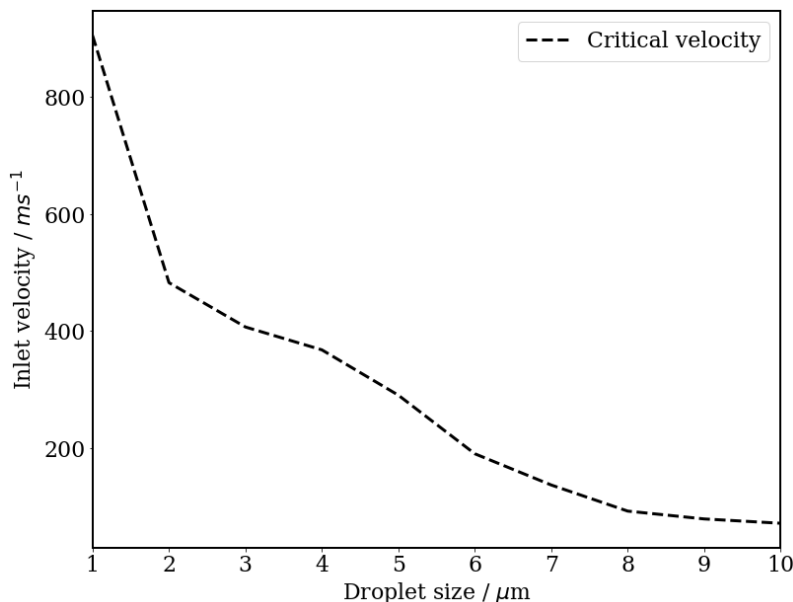


Figure 5.1: The critical detachment velocities for the 5 μm fibre with varying droplet size.

Figure 5.1 shows the velocity at which a particle will detach from a 5 μm fibre. As seen in figure 5.1, this critical velocity is much higher than those found with in a mask during a cough, suggesting that these smaller particles are unlikely to detach. This is contrast with the findings of Qian *et al.* [13] which

found that typically smaller particles re-aerosolise. One explanation for this might be that it is actually the larger particles which detach, but upon detachment they break up into smaller particles.

In figure 5.1 there is a trend downwards, suggesting that there is a droplet size at which the critical velocity is much lower. This is also in agreement with theory, as the droplet grows in size the drag force grows too. However, the surface tension which keeps the droplet attached to the fibre is limited by the fibre size. Thus, as the radius grows the detachment velocity decreases. This is also in alignment with Qian *et al.* [13, 14] in showing the clear dependence of detachment velocity on the size of the droplet itself.

Before this study, to determine the velocity through a mask a porous media model would have been used. Which, on average, gives a similar result to the models created in this study(figure 4.2). However, there are significant features in the flow which are lost when using these models. The work conducted here shows that these features do exist and when considering small scale simulations, like those of attachment and detachment, it is worth being mindful of them.

5.2 Packing density

Changing the packing density of the inner filtration layer had a significant affect on the flow. Plotting the data in table 4.1 clearly shows that as the packing density increases so do the linear and non-linear affects of the mask.

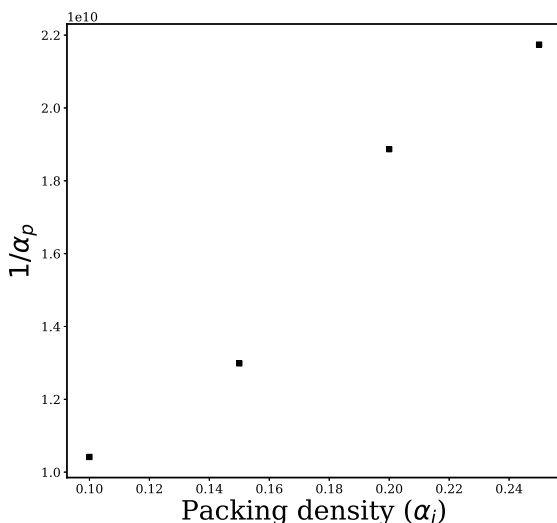


Figure 5.2: A plot of $\frac{1}{\alpha_p}$ against packing density.

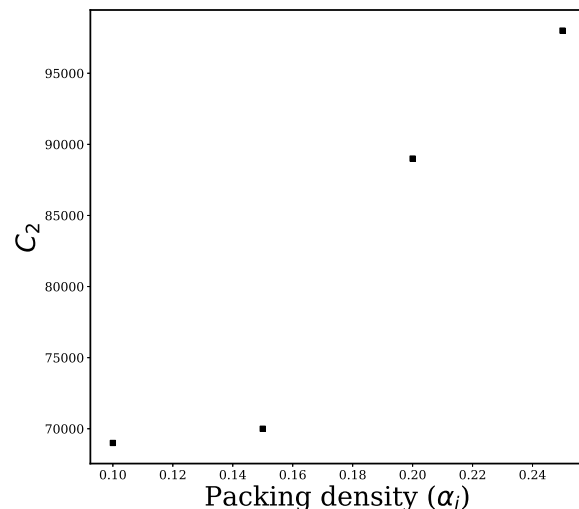


Figure 5.3: A plot of C_2 against packing density.

Being able to make these models allows larger scale simulations to utilise these smaller scale models. From this, the affect of using different materials, packing densities or fibre sizes can be assessed at a macro-scale. This allows other studies to directly connect changes at the macro-scale to those at a micro-scale.

The scripts used in this report can easily be adjusted to create a different material. All aspects of the geometry creation can be edited including: the number of layers, the fibre size and the domain size. As such this method can be used to model a vast range of masks. This flexibility shows the superiority of this method (virtual fibres) over other methods first considered [15, 16].

5.3 Limitations

In this work there were several limitations which made the geometry files less accurate than they could of been. First, when creating the geometry files the overlap between fibres is not accounted for. As such, some fibres occupy the same space but are accounted for twice when calculating the packing density. Due to this, the real packing density of the filter will be lower than that which is calculated. Abishek *et al.* [22] present a method in which this is accounted for by using an algorithm which moves the fibres such that the amount of these intersections are minimised. However, this was beyond the scope of this study.

When considering the masks on a slightly larger scale it can be seen that there are square melting junctions set between 500 μm and 1000 μm apart. These melting junctions can be seen in figure 5.4.

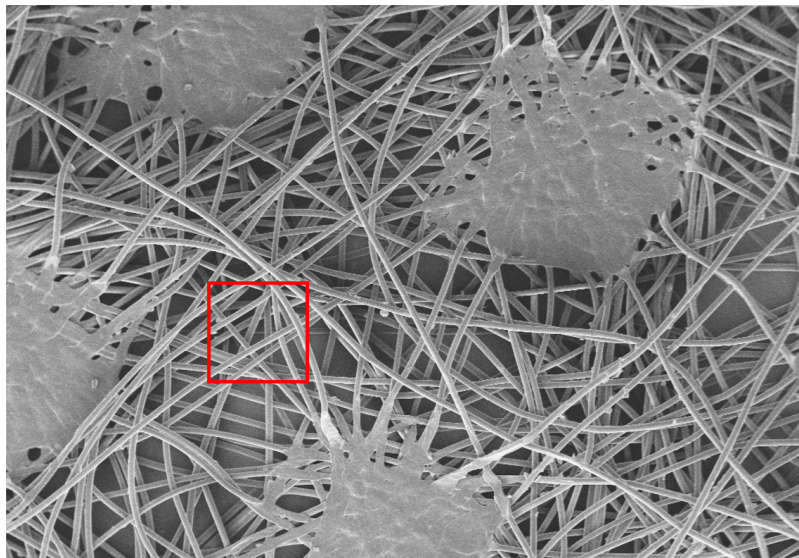


Figure 5.4: An SEM image of the outer layer of the mask, the melting junctions can be seen here. The red box highlights the size of the domain which has been simulated through out this report.

Since these features of the mask are not accounted for in the current model the real flow through a mask may differ somewhat to what is currently presented. Highlighted in red is the size of the domain which is currently being considered.

It is also possible that during prolonged used of a mask that the mask geometry itself may change. Also highlighted in Yatin's work is the amount of material which can collect on a mask through out prolonged use [20]. As can be seen in figures 5.5 & 5.6, a significant amount of material is collected on a mask during use. This effectively increases the packing density of the mask which should decrease the average velocity through the mask. This change in morphology of the fibres could significantly affect the flow profile.

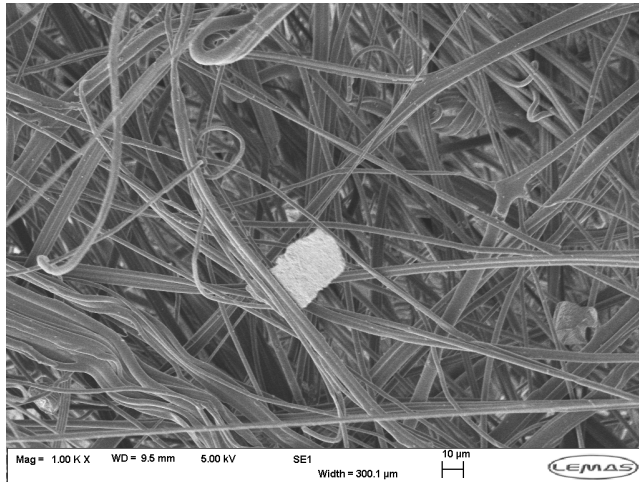


Figure 5.5: An SEM image of the inner layer of a used DFM.

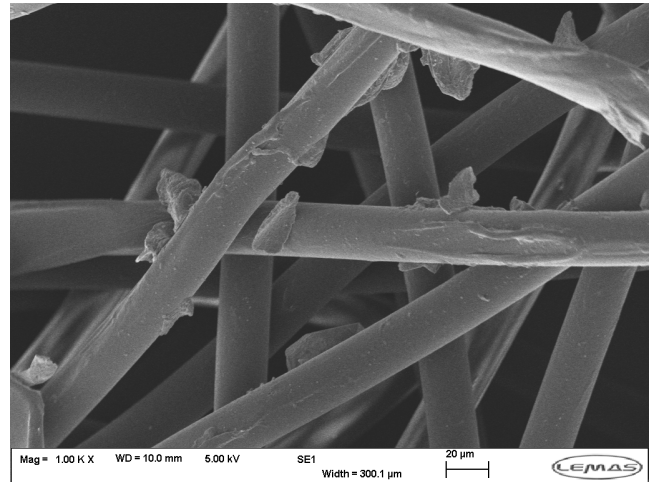


Figure 5.6: An SEM image of the outer layer of a used DFM.

Chapter 6

Conclusion

Currently presented in this study is a single phase simulation of air flow through a mask. However, now that this mask geometry has been generated it is possible to consider other, more complicated, problems. Ultimately, a mask prevents liquid droplets from entering the environment. An interesting avenue of enquiry would be looking at how a large droplet, of the order $80\text{ }\mu\text{m}$, interacts with mask fibres. It is possible that such a droplet breaks up into smaller droplets as it is pushed through the mask. This could perhaps explain the disparity found between the work of Quian *et al.* [13, 14] in comparison with the present study. The break up of such a droplet poses an interesting question. The process of attachment could also now be considered in light of the more complex flow fields found around mask fibres.

In previous work the link between re-aerosilisation and the velocity of the flow through the mask has been established [13, 14]. In order to model this using CFD, many studies opt for a porous jump boundary condition which utilises equation 2.2. This study has shown that these boundary conditions which deal with the mask are missing out on significant features of the flow. Although it is necessary to make these simplifications when conducting larger scale simulations, it is worth being mind-full that they are indeed approximations. For any problems, like droplet capture, for which the small scale needs to be resolved, these more complicated flow fields must be accounted for.

Bibliography

- [1] Mathilde Richard, Judith MA van den Brand, Theo M Bestebroer, Pascal Lexmond, Dennis de Meulder, Ron AM Fouchier, Anice C Lowen, and Sander Herfst. Influenza a viruses are transmitted via the air from the nasal respiratory epithelium of ferrets. *Nature communications*, 11(1):1–11, 2020.
- [2] Edward M Fisher, Aaron W Richardson, Shannon D Harpest, Kent C Hofacre, and Ronald E Shaffer. Reaerosolization of ms2 bacteriophage from an n95 filtering facepiece respirator by simulated coughing. *Annals of occupational hygiene*, 56(3):315–325, 2012.
- [3] Lydia Bourouiba. Turbulent gas clouds and respiratory pathogen emissions: potential implications for reducing transmission of covid-19. *Jama*, 323(18):1837–1838, 2020.
- [4] Manouk Abkarian, Simon Mendez, Nan Xue, Fan Yang, and Howard A Stone. Speech can produce jet-like transport relevant to asymptomatic spreading of virus. *Proceedings of the National Academy of Sciences*, 117(41):25237–25245, 2020.
- [5] Talib Dbouk and Dimitris Drikakis. On respiratory droplets and face masks. *Physics of fluids (1994)*, 32(6):63303–063303, 2020.
- [6] Department of Health & Social Care. Face coverings: when to wear one, exemptions, and how to make your own, 2021. Accessed: 11/06/2021.
- [7] Ali Khosronejad, Christian Santoni, Kevin Flora, Zexia Zhang, Seokkoo Kang, Seyedmehdi Payavash, and Fotis Sotiropoulos. Fluid dynamics simulations show that facial masks can suppress the spread of covid-19 in indoor environments. 2020.
- [8] Xiaotie Zhang, Hui Li, Shengnan Shen, and Mang Cai. Investigation of the flow-field in the upper respiratory system when wearing n95 filtering facepiece respirator. *Journal of occupational and environmental hygiene*, 13(5):372–382, 2016.

- [9] ZHIPENG LEI, James YANG, ZIQING ZHUANG, and Raymond ROBERGE. Simulation and evaluation of respirator faceseal leaks using computational fluid dynamics and infrared imaging. *The Annals of occupational hygiene*, 57(4):493–506, 2013.
- [10] De Yun Wang Jian Hua Zhu, Shu Jin Lee and Heow Pueh Lee. Evaluation of rebreathed air in human nasal cavity with n95 respirator: a cfd study. *Trauma and Emergency Care*, (4):15–18, 2016.
- [11] Vivek Kumar, Sravankumar Nallamothu, Sourabh Shrivastava, Harshrajsinh Jadeja, Pravin Nakod, Prem Andrade, Pankaj Doshi, and Guruswamy Kumaraswamy. On the utility of cloth facemasks for controlling ejecta during respiratory events. 2020.
- [12] Karen Leonas and Cindy Jones. The relationship of fabric properties and bacterial filtration efficiency for selected surgical face masks. *J Textile Apparel Tech Manage*, 3, 01 2003.
- [13] Yinge Qian, Klaus Willeke, Vidmantas Ulevicius, and Sergey A Grinshpun. Particle reentrainment from fibrous filters. *Aerosol Science and Technology*, 27(3):394–404, 1997.
- [14] Yinge Qian, Klaus Willeke, Sergey A Grinshpun, Jean Donnelly, and Christopher C Coffey. Performance of n95 respirators: filtration efficiency for airborne microbial and inert particles. *American Industrial Hygiene Association Journal*, 59(2):128–132, 1998.
- [15] Martin J Lehmann, Johannes Weber, Alexander Kilian, and Michael Heim. Microstructure simulation as part of fibrous filter media development processes - from real to virtual media. *Chemical engineering technology*, 39(3):403–408, 2016.
- [16] S Jaganathan, H Vahedi Tafreshi, and B Pourdeyhimi. Modeling liquid porosimetry in modeled and imaged 3-d fibrous microstructures. *Journal of colloid and interface science*, 326(1):166–175, 2008.
- [17] S Fotovati, H Vahedi Tafreshi, and B Pourdeyhimi. Influence of fiber orientation distribution on performance of aerosol filtration media. *Chemical engineering science*, 65(18):5285–5293, 2010.
- [18] Ryan Mead-Hunter, Andrew J.C King, Gerhard Kasper, and Benjamin J Mullins. Computational fluid dynamics (cfd) simulation of liquid aerosol coalescing filters. *Journal of aerosol science*, 61:36–49, 2013.
- [19] Benoit Maze, Hooman Vahedi Tafreshi, and Behnam Pourdeyhimi. Geometrical modeling of fibrous materials under compression. *Journal of applied physics*, 102(7):073533–073533–9, 2007.
- [20] Yatin Darbar. *An Experimental Investigation of the Reaerosolisation of Particles from a Face Mask*. 2021.

- [21] Daniele Battegazzore, Fulvia Cravero, and Alberto Frache. Is it possible to mechanical recycle the materials of the disposable filtering masks? *Polymers*, 12(11):1–18, 2020.
- [22] S Abishek, A.J.C King, R Mead-Hunter, V Golkarfar, W Heikamp, and B.J Mullins. Generation and validation of virtual nonwoven, foam and knitted filter (separator/coalescer) geometries for cfd simulations. *Separation and purification technology*, 188:493–507, 2017.
- [23] Alexander Lang. *Understanding the Performance of Face Masks and visualising there Effectiveness*. 2021.
- [24] Ciara Higham. *CFD Modelling of droplet detachment from a single face mask fibre*. 2021.